The role of charge recombination to triplet excitons in organic solar cells

https://doi.org/10.1038/s41586-021-03840-5

Received: 16 June 2020

Accepted: 20 July 2021

Published online: 29 September 2021

Check for updates

Alexander J. Gillett[1]✉, Alberto Privitera[2], Rishat Dilmurat[3], Akchheta Karki[4], Deping Qian[5], Anton Pershin[3,6], Giacomo Londi[3], William K. Myers[7], Jaewon Lee[4,8], Jun Yuan[5,9], Seo-Jin Ko[4,10], Moritz K. Riede[2], Feng Gao[5], Guillermo C. Bazan[4], Akshay Rao[1], Thuc-Quyen Nguyen[4]✉, David Beljonne[3]✉ & Richard H. Friend[1]✉

The use of non-fullerene acceptors (NFAs) in organic solar cells has led to power conversion efficiencies as high as 18%[1]. However, organic solar cells are still less efficient than inorganic solar cells, which typically have power conversion efficiencies of more than 20%[2]. A key reason for this difference is that organic solar cells have low open-circuit voltages relative to their optical bandgaps[3], owing to non-radiative recombination[4]. For organic solar cells to compete with inorganic solar cells in terms of efficiency, non-radiative loss pathways must be identified and suppressed. Here we show that in most organic solar cells that use NFAs, the majority of charge recombination under open-circuit conditions proceeds via the formation of non-emissive NFA triplet excitons; in the benchmark PM6:Y6 blend[5], this fraction reaches 90%, reducing the open-circuit voltage by 60 mV. We prevent recombination via this non-radiative channel by engineering substantial hybridization between the NFA triplet excitons and the spin-triplet charge-transfer excitons. Modelling suggests that the rate of back charge transfer from spin-triplet charge-transfer excitons to molecular triplet excitons may be reduced by an order of magnitude, enabling re-dissociation of the spin-triplet charge-transfer exciton. We demonstrate NFA systems in which the formation of triplet excitons is suppressed. This work thus provides a design pathway for organic solar cells with power conversion efficiencies of 20% or more.

In the Shockley–Queisser model, an ideal solar cell should have only radiative recombination, thus acting as an ideal light-emitting diode with 100% electroluminescence external quantum efficiency (EQE_{EL})[4,6–8]. This sets the limit on the photon energy loss ΔE_{loss}, which is defined as the difference between the optical bandgap and the energy of the extracted charges[4]. However, when $EQE_{EL} < 1$, non-radiative recombination incurs an additional voltage loss[7,8]:

$$\Delta V_{nr} = \frac{-k_B T}{q} \ln(EQE_{EL}), \quad (1)$$

where k_B is the Boltzmann constant, T is temperature, q is the elementary charge and ΔV_{nr} is the non-radiative voltage loss. In most NFA organic solar cells, EQE_{EL} is roughly 10^{-4}–10^{-5}, giving $\Delta V_{nr} \approx 230$–$290$ mV and $\Delta E_{loss} = 500$–600 meV (refs. [3,9–12]). Therefore, to achieve power conversion efficiencies of more than 20% in organic solar cells, ΔE_{loss} must be reduced[13,14], with ΔV_{nr} being the key area for improvement[13,15]. To better understand the factors that control EQE_{EL}, it is useful to separate the different contributions[16]:

$$EQE_{EL} = \gamma \Phi_{PL} \chi \eta_{out}, \quad (2)$$

where γ is the charge balance factor (often engineered to be 1), Φ_{PL} is the photoluminescence quantum efficiency, χ is the fraction of recombination events that decay radiatively (excitons in the spin-singlet configuration, S_1) and η_{out} is the photon out-coupling efficiency (typically about 0.3). Here, the two key factors that may be manipulated are Φ_{PL} and χ. For organic solar cells, we treat Φ_{PL} as being equivalent to the luminescence yield of spin-singlet excitations. In an efficient organic solar cell, almost all photo-generated spin-singlet excitons dissociate into free charges; photon emission occurs after free-charge recombination. Therefore, when recombination proceeds via the S_1 state of the component with the lowest optical bandgap[11,17], we consider that the Φ_{PL} for the neat (pure film) low-optical-bandgap material will set the upper limit on Φ_{PL} for the organic solar cell blend. Whereas recent empirical advances in EQE_{EL} have been achieved by increasing Φ_{PL}[11,13,18,19], here we consider the role of χ in NFA organic solar cells.

[1]Cavendish Laboratory, University of Cambridge, Cambridge, UK. [2]Clarendon Laboratory, University of Oxford, Oxford, UK. [3]Laboratory for Chemistry of Novel Materials, Université de Mons, Mons, Belgium. [4]Centre for Polymers and Organic Solids, Department of Chemistry and Biochemistry, University of California at Santa Barbara, Santa Barbara, CA, USA. [5]Department of Physics, Chemistry and Biology (IFM), Linköping University, Linköping, Sweden. [6]Wigner Research Centre for Physics, Budapest, Hungary. [7]Centre for Advanced Electron Spin Resonance, Inorganic Chemistry Laboratory, University of Oxford, Oxford, UK. [8]Department of Chemical Engineering and Applied Chemistry, Chungnam National University, Daejeon, South Korea. [9]College of Chemistry and Chemical Engineering, Central South University, Changsha, China. [10]Division of Advanced Materials, Korea Research Institute of Chemical Technology, Daejeon, South Korea. ✉e-mail: ajg216@cam.ac.uk; quyen@chem.ucsb.edu; david.beljonne@umons.ac.be; rhf10@cam.ac.uk

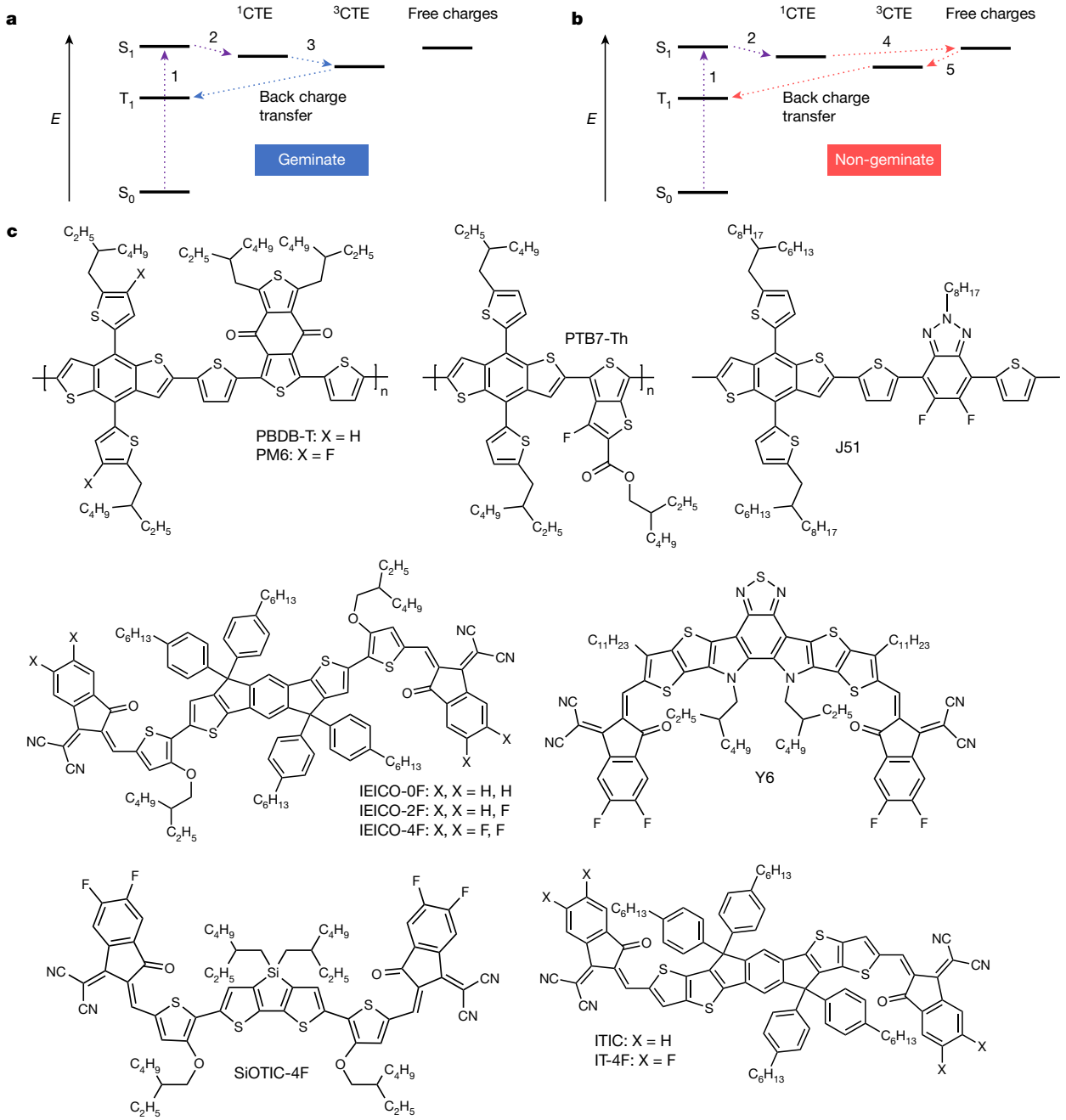

Fig. 1 | Triplet formation pathways and organic solar cell materials. **a**, Illustration of the geminate pathway for T_1 formation in organic solar cells. After optical excitation (1), charge transfer from the S_1 to the ^{1}CTE occurs (2). However, the ^{1}CTE does not separate into free charge before spin-mixing with the ^{3}CTE occurs (3; on nanosecond timescales). From the ^{3}CTE, back charge transfer to a lower-energy T_1 on either the donor or the acceptor may occur. **b**, Illustration of the non-geminate pathway for T_1 formation in organic solar cells. After optical excitation (1), charge transfer from the S_1 to ^{1}CTE occurs (2). The ^{1}CTE then dissociates in free charges (4), and the free charges undergo non-geminate recombination, forming a 3:1 ratio of ^{3}CTE and ^{1}CTE (5). From the ^{3}CTE, back charge transfer to a lower-energy T_1 on either the donor or the acceptor may occur. **c**, Molecular structures of the four polymer donors and seven NFA materials used in this study.

In organic solar cells, the recombination of free charges proceeds via the formation of charge-transfer excitons, with an electron on the acceptor material and a hole on the donor material. These charge-transfer excitons are created in a 1:3 ratio of spin-singlet (^{1}CTE) and spin-triplet (^{3}CTE) states via spin-statistical non-geminate recombination[20]. However, the organic solar cell systems studied so far have molecular triplet states (T_1) with lower energies than that of the ^{3}CTE on either the donor or the acceptor. Therefore, it is possible for back charge transfer from ^{3}CTE to T_1 to occur[21–23]. Because the S_1–T_1 energy gap in most organic semiconductors is around 0.6–1 eV[24], T_1 will have too low an energy to thermally re-dissociate into free charges and must decay non-radiatively[25], resulting in $\chi < 1$ and an increased ΔV_{nr}[26]. To understand whether a system will generate T_1, it is necessary to analyse the competing processes that may occur from the ^{3}CTE. This includes back charge transfer, re-dissociation into free charges and conversion to ^{1}CTE. We note that ^{3}CTE–^{1}CTE conversion, with a typical rate of 10^8–10^6 s^{-1}, is too slow to compete with the other pathways (see below)[27]. Thus, T_1 formation from ^{3}CTE is determined by the competition between the rates of back charge transfer (k_{BCT}) and re-dissociation ($k_{dissociation}$) of ^{3}CTE[22,28]. Furthermore, as ^{3}CTE may be

Table 1 | Key parameters for the organic solar cell blends

Blend	PCE (%)	$\Phi_{PL,NFA}$ (%)	EQE_{EL}	ΔV_{nr} (V)	Geminate T_1	Non-geminate T_1
PM6:Y6	15.2	1.3	4.3×10^{-5}	0.25	No	Yes
PM6:IT-4F	12.0	1.4	9.5×10^{-7}	0.35	No	Yes
PM6:ITIC	9.2	1.4	5.0×10^{-5}	0.25	No	Yes
PBDB-T:ITIC	11.2	1.4	8.8×10^{-7}	0.35	No	Yes
J51:ITIC	7.2	1.4	7.1×10^{-8}	0.42	No	Yes
PTB7-Th:SiOTIC-4F	8.9	<0.1	8.7×10^{-7}	0.35	No	Yes
PTB7-Th:IEICO-4F	10.2	0.4	1.6×10^{-6}	0.34	No	Yes
PTB7-Th:IEICO-2F	11.7	0.4	1.3×10^{-5}	0.28	No	No
PTB7-Th:IEICO-0F	7.2	0.6	1.4×10^{-4}	0.22	No	No

PCE, power conversion efficiency. Φ_{PL} was measured for a neat film of the NFA used in the blend. The error in Φ_{PL} is ±0.1%. For SiOTIC-4F, Φ_{PL} was too low to be measured and is therefore quoted as less than the smallest value reliably resolvable on our setup (0.1%). For the determination of ΔV_{nr}, EQE_{EL} at 293 K was taken at $-J_{SC}$ (short-circuit current density) to ensure that carrier densities were relevant to device operating conditions. Whether the blend forms triplet excitons that result from geminate and non-geminate recombination pathways is also indicated.

formed from geminate[29,30] (Fig. 1a) and from non-geminate[22,31,32] (Fig. 1b) charge-carrier pairs, it is also important to consider that back charge transfer to T_1 can occur through two distinct mechanisms.

T_1 generation is commonly observed and has been extensively studied in organic solar cells that use fullerenes as electron acceptors, although the effect on device performance is debated[22,26,29–31,33–35]. We consider the role of triplet states in NFA organic solar cells by examining nine high-performance systems. The structures of the four polymer donors and seven NFAs used in this study are shown in Fig. 1c. A summary of device performance (current density–voltage and EQE_{EL} curves are provided in Supplementary Figs. 2, 3), Φ_{PL} for a neat film of the relevant NFA, ΔV_{nr} and whether the blend exhibits geminate or non-geminate T_1 formation is given in Table 1. We find that geminate T_1 formation, as determined by transient electron paramagnetic resonance spectroscopy, is not observed in our NFA blends. However, non-geminate T_1 formation, probed through transient absorption spectroscopy, is usually seen, with the exception of the closely related PTB7-Th:IEICO-0F and PTB7-Th:IEICO-2F systems. Two NFA blends were selected to act as representative case studies: PM6:Y6, as one of the best-performing organic solar cell systems[5], despite exhibiting non-geminate T_1 formation, and PTB7-Th:IEICO-2F, which has no detectable back charge transfer to T_1. A full account of all other blends is provided in Supplementary Information.

In Fig. 2a, we show the transient absorption of PM6:Y6, pumped at 532 nm for preferential PM6 excitation. Here we focus solely on the infrared spectral region where the photo-induced absorptions of T_1 states are typically found (full-spectral-range data are provided in Supplementary Fig. 14)[22]. At 0.1–0.2 ps after excitation, we observe photo-induced absorption bands at 1,250 nm and 1,550 nm, which, after comparison with the transient absorption of the neat materials (Supplementary Figs. 5, 6), we assign to the PM6 S_1 and an intermolecular excitation between neighbouring Y6 molecules, respectively[36]. As charge transfer develops, these features are lost and a new photo-induced absorption at 1,450 nm grows beyond a few picoseconds, which we confirm to be the Y6 T_1 by using triplet sensitization experiments (Supplementary Fig. 4b). Kinetics from the T_1 spectral region (Fig. 2b) reveal a strong fluence dependence in T_1 formation, which demonstrates that triplets are generated via bimolecular processes. Deviation of the kinetics of the lowest and highest fluences in the T_1 region begins on sub-picosecond timescales, which demonstrates that non-geminate recombination occurs extremely quickly when the excitation fluence is high. From this, we infer that k_{BCT} for the interfacial ^{3}CTE must be around 10^{11}–10^{12} s^{-1}. To determine $k_{dissociation}$, we fitted the growth of the electro-absorption feature of the donor polymer in multiple blends (Supplementary Figs. 29–34); this growth is a signature of the separation of interfacial charge-transfer excitons into free charges[37–39]. The fitting reveals that $k_{dissociation}$ for the thermalized interfacial charge-transfer excitons in the PM6:Y6 blend is 6.3×10^{10} s^{-1}, with rates of between 10^{10} s^{-1} and 10^{11} s^{-1} found for the other NFA blends studied here. Therefore, we conclude that T_1 is observed in PM6:Y6 because $k_{BCT} \gg k_{dissociation}$. Furthermore, using an existing kinetic model (full details in Supplementary Information), we determine that around 90% of the recombination in this blend under conditions equivalent to open-circuit conditions (no charge carriers extracted from the film) proceeds non-radiatively via the Y6 T_1 (Supplementary Fig. 37). The T_1 recombination fraction may be greater than the 75% predicted by spin statistics because charge-transfer excitons form and separate multiple times before recombining[31,40]. We note that the presence of non-geminate T_1 formation in PM6:Y6 is representative of most NFA blends studied.

When recombination via T_1 is present, it accelerates the recombination of free charges via charge-transfer excitons by providing an additional deactivation pathway. However, it has been reported that the bimolecular recombination rates of efficient NFA organic solar cells are much less than the Langevin rate[41,42]. In our transient absorption measurements, we detect only the terminal recombination mechanism, not the preceding unsuccessful recombination attempts. Therefore, the high k_{BCT} that we measure is relevant for ^{3}CTE only at the donor–acceptor interface, where rapid back charge transfer to T_1 is favoured. Consistent with the large Langevin reduction factors reported, most recombination attempts must therefore take place at larger electron–hole separations, where $k_{dissociation} \gg k_{BCT}$, enablng rapid thermal ^{3}CTE re-dissociation. However, under open-circuit conditions, thermodynamics is the sole factor that determines ΔV_{nr}[7,8]. Thus, the only relevant consideration for ΔV_{nr} is the final state through which terminal recombination takes place, not the kinetics of the preceding processes.

We next use transient electron paramagnetic resonance spectroscopy to investigate geminate T_1 pathways. In Fig. 2c, we show the spectra of PM6:Y6 after 532-nm excitation (full discussion in Supplementary Fig. 53). At 1 µs, we observe a single, intense peak at 346 mT that is attributed to free charges[43] and a broader weak triplet feature. However, at 5 µs, there are no remaining triplet signals, probably owing to the rapid triplet-charge annihilation in this blend (Supplementary Fig. 38). The triplet detected at 1 µs may be simulated by a single eeeaaa ('e' = emission, 'a' = absorption) species, characteristic of T_1 formed via intersystem crossing mediated by spin–orbit coupling[23,44,45]. We attribute this T_1 to intersystem crossing from undissociated S_1 states. The absence of any triplet species with an aeeaae or eaaeea polarization pattern, a clear and unique fingerprint of the geminate back charge transfer pathway[23,44,45], confirms that geminate T_1 formation does not occur in this blend. This is a characteristic observation of all the NFA organic solar cell systems studied in our work.

We now focus on PTB7-Th:IEICO-2F, a NFA blend in which T_1 generation from charge-transfer excitons could not be detected; its transient absorption is shown in Fig. 2d (excitation at 620 nm preferentially pumped PTB7-Th). In the infrared spectral region (full-spectral-range data are provided in Supplementary Fig. 17), two distinct photo-induced absorption features (at 1,175 nm and 1,550 nm) are observed at the earliest time of 0.2–0.3 ps. After comparison with the transient absorption of the neat materials (Supplementary Figs. 7, 8), we assign the feature at 1,175 nm to the edge of the IEICO-2F S_1 and that at 1,550 nm to the PTB7-Th S_1. As charge transfer develops, both photo-induced absorptions are lost and only the edge of the photo-induced absorption of the PTB7-Th hole is visible (at 1,175 nm). There is no detectable formation of the photo-induced absorption of the IEICO-2F T_1, which is found to be at 1,350 nm from triplet sensitization measurements (Supplementary Fig. 4c). Furthermore, there is no fluence dependence of the kinetics taken from the IEICO-2F T_1 region (Fig. 2e), which provides additional evidence that non-geminate T_1 formation is not a detectable recombination pathway.

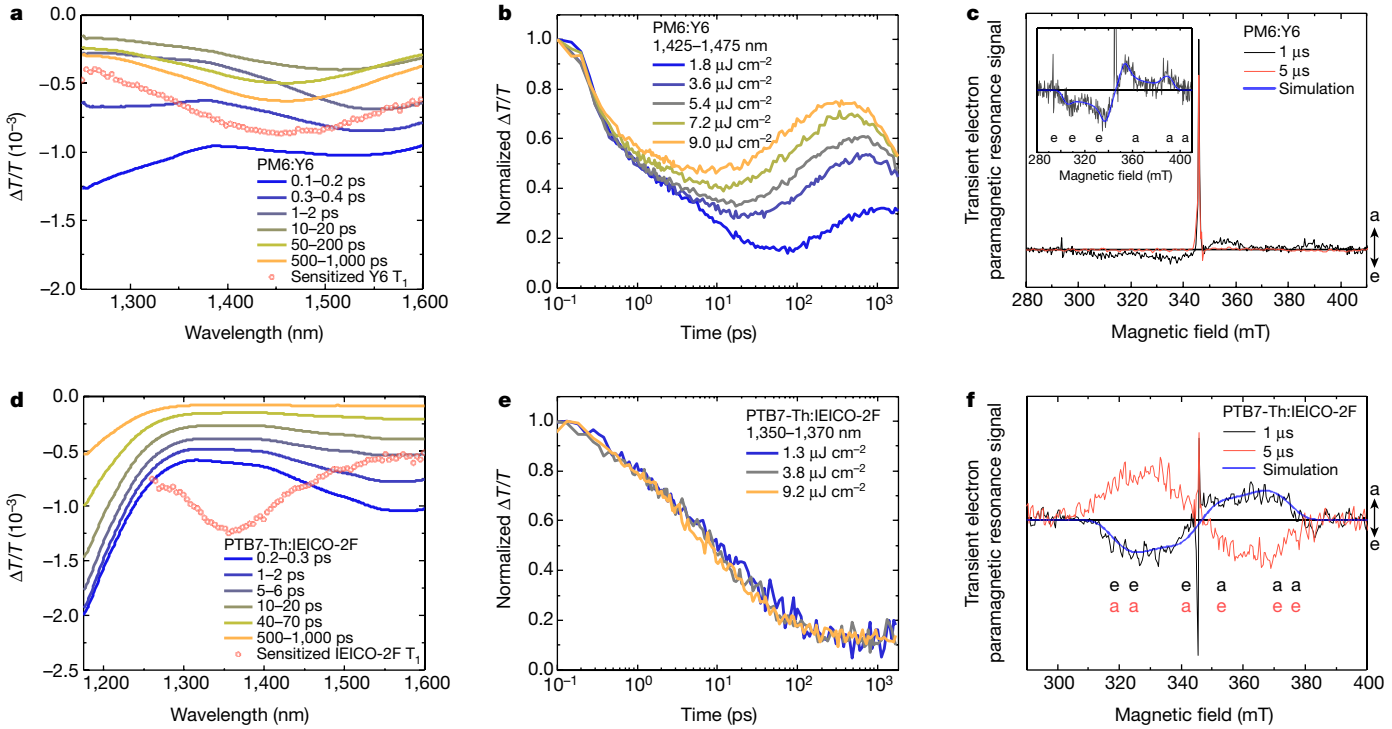

Fig. 2 | Spectroscopic investigations of triplet formation in model NFA blends. a, Transient absorption spectra in the infrared region of the PM6:Y6 blend (293 K), excited with a moderate fluence of 5.4 μJ cm^{-2} at 532 nm for preferential PM6 excitation. The Y6 T_1 photo-induced absorption forms at 1,450 nm, as confirmed by triplet sensitization experiments. **b**, Normalized transient absorption kinetics of the PM6:Y6 blend, taken around the maximum of the Y6 T_1 feature between 1,425 nm and 1,475 nm. The clear fluence dependence of T_1 formation is indicative of a bimolecular generation pathway. **c**, Transient electron paramagnetic resonance spectra of the PM6:Y6 blend (80 K) after excitation at 532 nm, taken at 1 μs and 5 μs. The inset shows a magnification and simulation of the weak signal that corresponds to the intersystem crossing triplet. The field positions of the absorption ('a') and emission ('e') transitions of the intersystem crossing triplet are indicated. **d**, Transient absorption spectra in the infrared region of the PTB7-Th:IEICO-2F blend (293 K), excited with a moderate fluence of 3.8 μJ cm^{-2} at 620 nm for preferential PTB7-Th excitation. The IEICO-2F T_1 photo-induced absorption at 1,350 nm does not form in the blend. **e**, Normalized transient absorption kinetics of the PTB7-Th:IEICO-2F blend, taken around the maximum of the IEICO-2F T_1 photo-induced absorption at 1,350–1,370 nm. No fluence dependence in the IEICO-2F T_1 region is observed. **f**, Transient electron paramagnetic resonance spectra of the PTB7-Th:IEICO-2F blend (80 K) after excitation at 532 nm, taken at 1 μs and 5 μs. The field positions of the absorption ('a') and emission ('e') transitions of the intersystem crossing triplet are indicated.

In the transient electron paramagnetic resonance of PTB7-Th:IEICO-2F excited at 532 nm (Fig. 2f; full discussion in Supplementary Fig. 57), we observe a prominent feature that corresponds to T_1 formed via intersystem crossing mediated by spin–orbit coupling; this feature has a clear eeeaaa polarization pattern, which inverts to aaaeee by 5 μs (refs. [23,44,45]). We also observe a ^{3}CTE with an ea polarization pattern at 346 mT, which evolves into free charges[23]. The T_1 spectral inversion by 5 μs is due to differing decay rates from the three high-field triplet levels[46]. To explain the increased intensity of the intersystem crossing T_1 in PTB7-Th:IEICO-2F, we note that the IEICO derivatives have relatively high intersystem crossing quantum yields of around 5% (Supplementary Fig. 35), which means that substantial T_1 formation from any undissociated S_1 is expected. However, geminate back charge transfer T_1 states are absent.

We next evaluate the effect of T_1 formation on device performance. In PM6:Y6, around 90% of the recombination under open-circuit conditions proceeds non-radiatively via the Y6 T_1; this equates to $\chi = 0.1$ in equation (2), which reduces EQE_{EL} by a factor of ten. From equation (1), this reduction in EQE_{EL} increases ΔV_{nr} by about 60 mV. We confirm this increase in ΔV_{nr} in the PTB7-Th:IEICO-2F and PTB7-Th:IEICO-4F blends; only PTB7-Th:IEICO-4F exhibits non-geminate T_1 formation (Supplementary Fig. 26), owing to a poorer energy alignment between ^{3}CTE and T_1 (Supplementary Fig. 66). Here, the NFA structures differ by only two fluorine atoms; the energies of the NFA S_1 are 1.36 eV and 1.34 eV for IEICO-2F and IEICO-4F, respectively, and those of the PTB7-Th-blend ^{1}CTE are 1.29 eV and 1.26 eV (Supplementary Fig. 62). The similarities between the molecular structures and Φ_{PL} of these two NFAs, as well as the electronic properties of their blend with PTB7-Th, enable a direct appraisal of the contribution from T_1 formation to ΔV_{nr}[17,47]. $\Delta V_{nr} = 0.28$ V is obtained for PTB7-Th:IEICO-2F, whereas $\Delta V_{nr} = 0.34$ V is found for PTB7-Th:IEICO-4F (Supplementary Fig. 3), consistent with our estimate of extra losses of roughly 60 mV from substantial recombination via T_1.

For the blends presented here, we find the largest ΔV_{nr} ($\Delta V_{nr} \geq 0.35$ V) in systems with large S_1–^{1}CTE offsets and recombination via T_1 (PM6:IT-4F, PBDB-T:ITIC, J51:ITIC; Table 1). Owing to the large S_1–^{1}CTE energy gap, thermal reactivation from ^{1}CTE to the bright NFA S_1 state is not efficient[17,42]. Consequently, the primary radiative pathway available is via the ^{1}CTE, for which Φ_{PL} is roughly 100 times lower than for the NFA S_1[17]. The blends with smaller ΔV_{nr} ($\Delta V_{nr} < 0.35$ V) have reduced S_1–^{1}CTE gaps. In low-offset systems, ΔV_{nr} is particularly sensitive to the S_1–^{1}CTE energy gap[17]. However, we can generally explain the observed ΔV_{nr} using Φ_{PL} for the NFA and the presence or absence of recombination via T_1. For example, PM6:Y6 and PTB7-Th:IEICO-0F both have an S_1–^{1}CTE offset of about 50 meV (Supplementary Fig. 63). However, despite the much lower Φ_{PL} (0.6%) for IEICO-0F than for Y6 (1.3%), we report a lower ΔV_{nr} ($\Delta V_{nr} = 0.22$ V) in PTB7-Th:IEICO-0F ($\Delta V_{nr} = 0.25$ V for PM6:Y6). Therefore, the improved ΔV_{nr} may be attributed directly to the suppressed recombination via T_1 in PTB7-Th:IEICO-0F.

To optimize power conversion efficiencies, organic solar cells should be designed to avoid T_1 formation. We therefore explore the role of intermolecular interactions between donors and acceptors

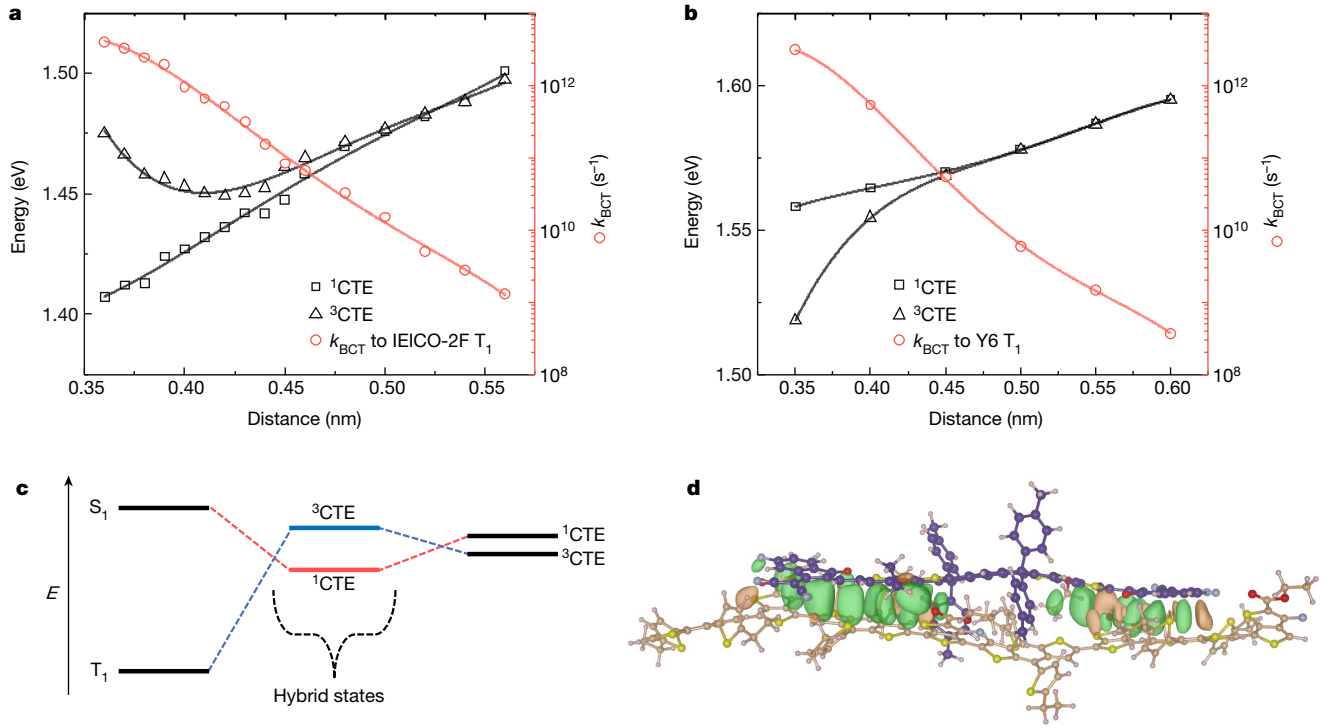

Fig. 3 | The role of hybridization in organic solar cell blends. a, **b**, Results of a rigid scan of the ^{1}CTE and ^{3}CTE energies for representative PTB7-Th:IEICO-2F (**a**) and PM6:Y6 (**b**) supramolecular configurations as a function of donor–acceptor separation (black; left axis). At each donor–acceptor separation, k_{BCT} for ^{3}CTE to T_1 of the NFA is also displayed (red; right axis). The solid lines are best-fit polynomial guides to the eye. **c**, Schematic of the effect of hybridization between charge-transfer and local excitons on the energetic ordering of the ^{1}CTE and the ^{3}CTE. **d**, The optimized supramolecular configuration between PTB7-Th (beige) and IEICO-2F (purple) used for the calculations in **a**. The lobes represent regions of constructive overlap between the highest occupied molecular orbitals of the donor and the acceptor. This overlap controls the size of the electronic coupling and thus mediates the hybridization between the local excitons of the NFA and the charge-transfer excitons; for hybridization between the local excitons of the donor polymer and the charge-transfer excitons, the overlap between the lowest occupied molecular orbitals is the relevant interaction.

in T_1 generation through quantum-chemical calculations. Beginning with PTB7-Th:IEICO-2F, we calculate the ^{1}CTE and ^{3}CTE energies at the equilibrium donor–acceptor geometry. We find that the energy ordering of the charge-transfer excitons is inverted from that expected when considering the electron-exchange interaction[24], with the energy of the ^{3}CTE higher than that of the ^{1}CTE by around 70 meV. We next calculate the ^{1}CTE and ^{3}CTE excitation energies as a function of donor–acceptor separation. The results displayed in Fig. 3a show that, below 0.5 nm, the ^{1}CTE is rapidly stabilized, whereas the ^{3}CTE is destabilized. By contrast, the PM6:Y6 configurations that we explored have the expected ordering, with ^{1}CTE above ^{3}CTE (Fig. 3b, Supplementary Fig. 66). By analysing the excited-state wavefunctions, we conclude that the inversion of ^{1}CTE and ^{3}CTE in PTB7-Th:IEICO-2F arises from hybridization between the charge-transfer and local excitons[11,18,19]. Inversion occurs because the NFA S_1 has higher energy than the ^{1}CTE and because the NFA T_1 has lower energy than the ^{3}CTE; hybridization of these states therefore stabilizes the ^{1}CTE and destabilizes the ^{3}CTE (Fig. 3c). The primary reason for hybridization is the enhanced electronic coupling in the PTB7-Th:IEICO-2F complex; this enhanced coupling is due to (i) the similar bonding–antibonding pattern of the highest occupied molecular orbitals, with the same sequence of vertical nodal planes along the main molecular axis (Fig. 3d, Supplementary Fig. 70), and (ii) the near-perfect registry between the NFA and the polymer backbone, which provide substantial molecular overlap (Supplementary Fig. 65). The PM6 and Y6 combination does not have these attributes and hence does not exhibit hybridization between the charge-transfer and local excitons. In addition, we find excellent agreement between our calculations and experimental observations, with back charge transfer T_1 formation suppressed only in the blends that exhibit substantial hybridization between charge-transfer and local excitons (Fig. 3a, b, Supplementary Fig. 67).

The consequence of hybridization destabilizing the ^{3}CTE at close donor–acceptor separations is that it causes the electron and hole to remain more distant in the spin-triplet configuration, effectively increasing the interfacial ^{3}CTE radius. Because the donor–acceptor electronic coupling, and thus k_{BCT}, decreases exponentially with distance[48], it provides additional time for the thermal re-dissociation of ^{3}CTE[49]. Our calculations of the energy of the charge-transfer excitons as a function of intermolecular separation for the PTB7-Th:IEICO-2F complex indicate that hybridization between charge-transfer and local excitons results in a new ^{3}CTE energetic minima at a donor–acceptor stacking distance of 0.42 nm. When comparing k_{BCT} for the IEICO-2F T_1 at 0.42 nm and 0.35 nm, we observe that it is reduced by an order of magnitude, from about 10^{12} s^{-1} to about 10^{11} s^{-1} (Fig. 3a). Consistent with our experimental observations in which the NFA T_1 is populated via back charge transfer, we find that k_{BCT} for the NFA is consistently higher when the donor-polymer T_1 is energetically accessible from ^{3}CTE (Supplementary Fig. 64). Critically, the $k_{dissociation}$ of between 10^{10} s^{-1} and 10^{11} s^{-1} that we observe experimentally in our NFA organic solar cells is comparable to the reduced k_{BCT} enabled by hybridization between charge-transfer and local excitons. This finding confirms that hybridization is a feasible route to suppressing back charge transfer to T_1. In thin films of organic semiconductors, there will be a range of intermolecular stacking distances (broadly centred around roughly 0.38 nm in conjugated polymers) due to disorder induced by the side chains[50]. Thus, our calculations suggest that in a real-world organic solar cell blend the ^{3}CTE excitations will preferentially locate at lower-energy interfacial sites with increased donor–acceptor stacking distances and reduced k_{BCT}.

From these observations, we suggest design rules that encourage hybridization between (triplet) charge-transfer and local excitons in organic solar cell blends: (i) close energy resonance (preferably less than 100 meV) between the interacting local and charge-transfer exciton states; (ii) strong overlap and phase matching between the interacting frontier molecular orbital wavefunctions of the donor and the acceptor; and (iii) spatial registry between the donor and acceptor materials, to allow for the close intermolecular contacts necessary for strong wavefunction interactions.

Although the importance of optimizing Φ_{PL} in organic solar cells is already well known[13], the insight provided by this work demonstrates the critical role of T_1 states for ΔE_{loss}. If T_1 formation is suppressed, with ^{3}CTE–T_1 hybridization providing one viable pathway, then ΔE_{loss} may be reduced by about 60 meV, enough to enable power conversion efficiencies of 20% with the current best device-performance metrics[13,14]. Therefore, future development of organic solar cells should focus on simultaneously increasing Φ_{PL} and engineering out T_1 formation. To this end, quantum-chemical calculations of the electronic interactions between the donor and acceptor could provide a predictive tool for screening prospective donor–acceptor pairs. We also anticipate that the spin control over charge recombination demonstrated here will be of interest to the broader field of excitonic semiconductors.

Online content

Any methods, additional references, Nature Research reporting summaries, source data, extended data, supplementary information, acknowledgements, peer review information; details of author contributions and competing interests; and statements of data and code availability are available at https://doi.org/10.1038/s41586-021-03840-5.

1. Liu, Q. et al. 18% efficiency organic solar cells. *Sci. Bull.* **65**, 272–275 (2020).
2. Green, M. A. et al. Solar cell efficiency tables (version 55). *Prog. Photovolt. Res. Appl.* **28**, 3–15 (2020).
3. Liu, S. et al. High-efficiency organic solar cells with low non-radiative recombination loss and low energetic disorder. *Nat. Photon.* **14**, 300–305 (2020).
4. Menke, S. M., Ran, N. A., Bazan, G. C. & Friend, R. H. Understanding energy loss in organic solar cells: toward a new efficiency regime. *Joule* **2**, 25–35 (2018).
5. Yuan, J. et al. Single-junction organic solar cell with over 15% efficiency using fused-ring acceptor with electron-deficient core. *Joule* **3**, 1140–1151 (2019).
6. Shockley, W. & Queisser, H. J. Detailed balance limit of efficiency of p–n junction solar cells. *J. Appl. Phys.* **32**, 510–519 (1961).
7. Ross, R. T. Some thermodynamics of photochemical systems. *J. Chem. Phys.* **46**, 4590–4593 (1967).
8. Rau, U. Reciprocity relation between photovoltaic quantum efficiency and electroluminescent emission of solar cells. *Phys. Rev. B* **76**, 085303 (2007).
9. Lee, J. et al. Design of nonfullerene acceptors with near-infrared light absorption capabilities. *Adv. Energy Mater.* **8**, 1801209 (2018).
10. Cui, Y. et al. Over 16% efficiency organic photovoltaic cells enabled by a chlorinated acceptor with increased open-circuit voltages. *Nat. Commun.* **10**, 2515 (2019).
11. Qian, D. et al. Design rules for minimizing voltage losses in high-efficiency organic solar cells. *Nat. Mater.* **17**, 703–709 (2018).
12. Zhou, Z. et al. Subtle molecular tailoring induces significant morphology optimization enabling over 16% efficiency organic solar cells with efficient charge generation. *Adv. Mater.* **32**, 1906324 (2020).
13. Li, S., Li, C., Shi, M. & Chen, H. New phase for organic solar cell research: emergence of Y-series electron acceptors and their perspectives. *ACS Energy Lett.* **5**, 1554–1567 (2020).
14. Yuan, J. et al. Reducing voltage losses in the A-DA′D-A acceptor-based organic solar cells. *Chem* **6**, 2147–2161 (2020).
15. Vandewal, K., Mertens, S., Benduhn, J. & Liu, Q. The cost of converting excitons into free charge carriers in organic solar cells. *J. Phys. Chem. Lett.* **11**, 129–135 (2020).
16. Geffroy, B., le Roy, P. & Prat, C. Organic light-emitting diode (OLED) technology: materials, devices and display technologies. *Polym. Int.* **55**, 572–582 (2006).
17. Classen, A. et al. The role of exciton lifetime for charge generation in organic solar cells at negligible energy-level offsets. *Nat. Energy* **5**, 711–719 (2020).
18. Eisner, F. D. et al. Hybridization of local exciton and charge-transfer states reduces nonradiative voltage losses in organic solar cells. *J. Am. Chem. Soc.* **141**, 6362–6374 (2019).
19. Chen, X.-K., Coropceanu, V. & Brédas, J.-L. Assessing the nature of the charge-transfer electronic states in organic solar cells. *Nat. Commun.* **9**, 5295 (2018).
20. Wang, J., Chepelianskii, A., Gao, F. & Greenham, N. C. Control of exciton spin statistics through spin polarization in organic optoelectronic devices. *Nat. Commun.* **3**, 1191 (2012).
21. Chen, X.-K., Wang, T. & Brédas, J.-L. Suppressing energy loss due to triplet exciton formation in organic solar cells: the role of chemical structures and molecular packing. *Adv. Energy Mater.* **7**, 1602713 (2017).
22. Rao, A. et al. The role of spin in the kinetic control of recombination in organic photovoltaics. *Nature* **500**, 435–439 (2013).
23. Kraffert, F. et al. Charge separation in PCPDTBT:PCBM blends from an EPR perspective. *J. Phys. Chem. C* **118**, 28482–28493 (2014).
24. Köhler, A. & Beljonne, D. The singlet–triplet exchange energy in conjugated polymers. *Adv. Funct. Mater.* **14**, 11–18 (2004).
25. Hodgkiss, J. M. et al. Exciton-charge annihilation in organic semiconductor films. *Adv. Funct. Mater.* **22**, 1567–1577 (2012).
26. Benduhn, J. et al. Impact of triplet excited states on the open-circuit voltage of organic solar cells. *Adv. Energy Mater.* **8**, 1800451 (2018).
27. Cohen, A. E. Nanomagnetic control of intersystem crossing. *J. Phys. Chem. A* **113**, 11084–11092 (2009).
28. Shoaee, S. et al. Decoding charge recombination through charge generation in organic solar cells. *Sol. RRL* **3**, 1900184 (2019).
29. Dimitrov, S. D. et al. Polaron pair mediated triplet generation in polymer/fullerene blends. *Nat. Commun.* **6**, 6501 (2015)
30. Salvadori, E. et al. Ultra-fast spin-mixing in a diketopyrrolopyrrole monomer/fullerene blend charge transfer state. *J. Mater. Chem. A* **5**, 24335–24343 (2017).
31. Menke, S. M. et al. Limits for recombination in a low energy loss organic heterojunction. *ACS Nano* **10**, 10736–10744 (2016).
32. Xue, L. et al. Side chain engineering on medium bandgap copolymers to suppress triplet formation for high-efficiency polymer solar cells. *Adv. Mater.* **29**, 1703344 (2017).
33. Chow, P. C. Y., Gélinas, S., Rao, A. & Friend, R. H. Quantitative bimolecular recombination in organic photovoltaics through triplet exciton formation. *J. Am. Chem. Soc.* **136**, 3424–3429 (2014).
34. Di Nuzzo, D. et al. Improved film morphology reduces charge carrier recombination into the triplet excited state in a small bandgap polymer-fullerene photovoltaic cell. *Adv. Mater.* **22**, 4321–4324 (2010).
35. Karuthedath, S. et al. Buildup of triplet-state population in operating TQ1:$PC_{71}BM$ devices does not limit their performance. *J. Phys. Chem. Lett.* **11**, 2838–2845 (2020).
36. Wang, R. et al. Charge separation from an intra-moiety intermediate state in the high-performance PM6:Y6 organic photovoltaic blend. *J. Am. Chem. Soc.* **142**, 12751–12759 (2020).
37. Gelinas, S. et al. Ultrafast long-range charge separation in organic semiconductor photovoltaic diodes. *Science* **343**, 512–516 (2014).
38. Jakowetz, A. C. et al. Visualizing excitations at buried heterojunctions in organic semiconductor blends. *Nat. Mater.* **16**, 551–557 (2017).
39. Menke, S. M. et al. Order enables efficient electron-hole separation at an organic heterojunction with a small energy loss. *Nat. Commun.* **9**, 277 (2018).
40. Burke, T. M., Sweetnam, S., Vandewal, K. & McGehee, M. D. Beyond langevin recombination: how equilibrium between free carriers and charge transfer states determines the open-circuit voltage of organic solar cells. *Adv. Energy Mater.* **5**, 1500123 (2015).
41. Hosseini, S. M. et al. Putting order into PM6:Y6 solar cells to reduce the Langevin recombination in 400 nm thick junction. *Sol. RRL* **4**, 2000498 (2020).
42. Karki, A. et al. Understanding the high performance of over 15% efficiency in single-junction bulk heterojunction organic solar cells. *Adv. Mater.* **31**, 1903868 (2019).
43. Niklas, J. et al. Highly-efficient charge separation and polaron delocalization in polymer-fullerene bulk-heterojunctions: a comparative multi-frequency EPR and DFT study. *Phys. Chem. Chem. Phys.* **15**, 9562–9574 (2013).
44. Richert, S., Tait, C. E. & Timmel, C. R. Delocalisation of photoexcited triplet states probed by transient EPR and hyperfine spectroscopy. *J. Magn. Reson.* **280**, 103–116 (2017).
45. Thomson, S. A. J. et al. Charge separation and triplet exciton formation pathways in small molecule solar cells as studied by time-resolved EPR spectroscopy. *J. Phys. Chem. C* **121**, 22707–22719 (2017).
46. Hintze, C., Steiner, U. E. & Drescher, M. Photoexcited triplet state kinetics studied by electron paramagnetic resonance spectroscopy. *ChemPhysChem* **18**, 6–16 (2017).
47. Benduhn, J. et al. Intrinsic non-radiative voltage losses in fullerene-based organic solar cells. *Nat. Energy* **2**, 17053 (2017).
48. Kubas, A. et al. Electronic couplings for molecular charge transfer: benchmarking CDFT, FODFT and FODFTB against high-level ab initio calculations. II. *Phys. Chem. Chem. Phys.* **17**, 14342–14354 (2015).
49. Chang, W. et al. Spin-dependent charge transfer state design rules in organic photovoltaics. *Nat. Commun.* **6**, 6415 (2015).
50. Street, R. A., Song, K. W., Northrup, J. E. & Cowan, S. Photoconductivity measurements of the electronic structure of organic solar cells. *Phys. Rev. B* **83**, 165207 (2011).

Publisher's note Springer Nature remains neutral with regard to jurisdictional claims in published maps and institutional affiliations.

© The Author(s), under exclusive licence to Springer Nature Limited 2021

Methods

Rate equations for the processes that control triplet formation in organic solar cell blends

If back charge transfer proceeds to the electron acceptor, k_{BCT} and $k_{dissociation}$ may be defined as[51]

$$^3[D^+][A^-] \xrightarrow{k_{BCT}} {}^1_0[D] + {}^3_1[A], \quad (3)$$

$$^3[D^+][A^-] \xrightarrow{k_{dissociation}} [D^+] + [A^-], \quad (4)$$

where $[D^+]$ is the free hole on the donor component, $[A^-]$ is the free electron on the acceptor material, $^3[D^+][A^-]$ represents the coulombically bound ^{3}CTE, $^1_0[D]$ is the spin-singlet ground state of the donor and $^3_1[A]$ is the T_1 of the acceptor. The conversion of ^{3}CTE back into ^{1}CTE occurs primarily via hyperfine coupling, typically taking place with a rate of 10^8–10^6 s^{-1} in organic semiconductors[27]; this is much slower than the k_{BCT} and $k_{dissociation}$ determined here, which are both of the order of 10^{10}–10^{12} s^{-1}. The rate of the hyperfine-coupling-induced ^{3}CTE–^{1}CTE interconversion process (k_{HFC}) is

$$^3[D^+][A^-] \xrightarrow{k_{HFC}} {}^1[D^+][A^-], \quad (5)$$

where $^1[D^+][A^-]$ represents the coulombically bound ^{1}CTE. In addition to the primary geminate and non-geminate pathways that occur via charge-transfer excitons, T_1 formation via direct spin–orbit coupling intersystem crossing from undissociated S_1 states may also be considered a geminate T_1 formation mechanism, and is the only geminate pathway detected in the transient electron paramagnetic resonance (trEPR) measurements of our NFA blends. However, because it requires S_1 to remain undissociated, it will not be an important pathway in blends that exhibit efficient exciton dissociation and good device performance. The rate of intersystem crossing (k_{ISC}) from S_1 to T_1, defined here for the acceptor component, is

$$^1_1[A] \xrightarrow{k_{ISC}} {}^3_1[A], \quad (6)$$

where $^1_1[A]$ is the S_1 of the acceptor.

Organic solar cell device fabrication

Indium tin oxide (ITO)-patterned glass substrates were cleaned by scrubbing with soapy water, followed by sonication in soapy water, deionized water, acetone and isopropanol for 20 min each. The substrates were dried using compressed nitrogen and placed in an oven overnight at 100 °C. The conventional architecture devices were made by treating the ITO substrates with UV-ozone for 15 min and spin-coating a layer of poly(3,4-ethylenedioxythiophene):poly(styrenesulfonate) (PEDOT:PSS, Clevios P VP Al 8043) at 3,000 rpm for 40 s onto the ITO substrates in air. The substrates were then annealed in air at 150 °C for 20 min. Active layers were spin-coated on top of the PEDOT:PSS layer inside a nitrogen-filled glovebox. The substrates were then pumped down under vacuum (less than 10^{-7} torr), and a 5-nm-thick Ca interlayer followed by a 100-nm-thick Al electrode were deposited on top of the active layer by thermal evaporation using the Angstrom Engineering Series EQ Thermal Evaporator. In the case of inverted architecture devices, ZnO was used as the bottom transparent electrode (replacing PEDOT:PSS), with the ZnO solution prepared in a nitrogen glovebox by mixing tetrahydrofuran and diethylzinc (2:1). The fresh ZnO solution was then spin-coated on top of the clean ITO substrates at 4,000 rpm for 30 s and then placed on a hotplate at 110 °C for 15 min. Following active-layer spin-coating, the inverted devices were pumped down under vacuum (less than 10^{-7} torr), and 7 nm of MoO_x and a 100-nm-thick Ag electrode were deposited on top of the active layer by thermal evaporation. The electrode overlap area was 0.22 cm^2 for conventional and inverted devices. The active area of the device was determined using an optical microscope. The optimized active-layer compositions used for the blend solutions were based on previously published reports[9,42,52].

Organic solar cell device testing

Photovoltaic characteristic measurements were carried out inside a N_2-filled glovebox. Solar cell device properties were measured under illumination by a simulated 100 mW cm^{-2} AM1.5 G light source using a 300-W Xe arc lamp with an AM1.5 global filter. The irradiance was adjusted to 1 Sun with a standard silicon photovoltaic cell calibrated by the National Renewable Energy Laboratory. No spectral mismatch correction was applied. A Keithley 2635A source measurement unit was used to scan the voltage applied to the solar cell between −2 V and 1 V at a speed of 0.43 V s^{-1} with a dwell time of 46 ms. Scans were performed in the forward and reverse directions, with no unusual behaviour observed. Between eight and 30 individual solar cell devices were tested for each blend reported. The error associated with the reported power conversion efficiencies is ±0.2%.

Electroluminescence and EQE_{EL} measurements

Electroluminescence measurements were performed using one of two setups, depending on the wavelength range of interest. For measurements under 1,050 nm, a custom-made electroluminescence spectrometer was used. The electroluminescence emission from a sample driven by a Keithley source-measure unit (model 2602A) was collected by a lens system and focused on the entrance slit of a spectrograph (Acton Research SP-500) equipped with a Si charge-coupled detector (Princeton Instruments Pixis:400). The spectra collected by the detector were corrected for the instrument response function. The correction factors were determined by measuring the spectrum of a black-body-like light source (Ocean Optics LS-1). For electroluminescence measurements in the range 900–1,700 nm, we used a Photon Technology International (PTI) Quantamaster fluorimeter equipped with an Edinburgh Instruments EI-L Ge detector. The excitation monochromator of the fluorimeter was not used, and the electroluminescence emission was generated by driving the devices by a Keithley 2602 source-measure unit. An optical chopper (Thorlabs MC2000) was placed in front of the emission monochromator to make use of the fluorimeter's lock-in-amplifier-based detection system. The PTI Felix fluorimeter software was used for the data collection and correction of the instrumental artefacts. The efficiency of electroluminescence was obtained by applying a bias from −1 V to 2 V with a dual-channel Keithley 2602 to the solar cell and placing a silicon or germanium photodiode directly in front of it to collect the emission as a function of applied bias. The current running through the device and the photodiode were simultaneously measured.

Photoluminescence quantum efficiency measurements

The photoluminescence quantum efficiency was determined using a method described previously[53]. Samples were placed in an integrating sphere and photoexcited using a 658-nm continuous-wave laser. The laser and emission signals were measured and quantified using calibrated Andor iDus DU420A BVF Si and Andor CCD-1430 InGaAs detectors.

Transient absorption (TA) spectroscopy

In TA, T_1 states often have distinct photo-induced absorption features, enabling unambiguous assignment. By investigating the fluence dependence of the T_1 dynamics, we can readily determine whether formation follows the bimolecular kinetics expected for non-geminate recombination[22] or the monomolecular kinetics anticipated if T_1 is produced from geminate processes[29]. We can also quantify the T_1 population (N_T) directly from the TA signal through knowledge of the T_1 absorption cross section (σ_T), corresponding to the TA signal produced by a single T_1 state[54]: $\Delta T/T = \sigma_T N_T$ (see Supplementary Information for more details).

Samples for TA measurements were fabricated by spin-coating solutions onto quartz substrates using identical conditions to the optimized devices. The samples were encapsulated in a nitrogen glovebox environment to ensure oxygen-free measurements.

TA was performed on one of two experimental setups. The broadband-probe (525–1,650 nm) TA was performed on a setup powered using a commercially available Ti:sapphire amplifier (Spectra Physics Solstice Ace). The amplifier operates at 1 kHz and generates 100-fs pulses centred at 800 nm with an output of 7 W. A TOPAS optical parametric amplifier was used to provide the tuneable, roughly 100-fs pump pulses for the 'short time' (100 fs–1.8 ns) TA measurements, while the second harmonic (532 nm) of an electronically triggered, Q-switched Nd:YVO_4 laser (Advanced Optical Technologies AOT-YVO-25QSPX) provided the roughly 1-ns pump pulses for the 'long time' (1 ns–100 µs) TA measurements. The probe was provided by broadband visible (525–775 nm), near-infrared (800–1,200 nm) and infrared (1,250–1,650 nm) non-collinear optical parametric amplifiers (NOPAs). The probe pulses were collected with an InGaAs dual-line array detector (Hamamatsu G11608-512DA), driven and read out by a custom-built board from Stresing Entwicklungsbüro. The probe beam was split into two identical beams by a 50/50 beam splitter. This allowed the use of a second reference beam, which also passes through the sample but does not interact with the pump. The role of the reference was to correct for any shot-to-shot fluctuations in the probe that would otherwise greatly increase the structured noise in our experiments. Through this arrangement, very small signals with $\Delta T/T = 1 \times 10^{-5}$ could be measured.

For the 500–950-nm continuous-probe-region TA, a Yb amplifier (PHAROS, Light Conversion), operating at 38 kHz and generating 200-fs pulses centred at 1,030 nm with an output of 14.5 W was used. The roughly 200-fs pump pulse was provided by a TOPAS optical parametric amplifier. The probe is provided by a white-light supercontinuum generated in a YAG crystal from a small amount of the 1,030-nm fundamental. After passing through the sample, the probe is imaged using a Si photodiode array (Stresing S11490). This setup provided additional flexibility by allowing for broadband spectrum acquisition in one measurement, as well as a good signal-to-noise ratio in the 750–850-nm region, which is difficult to obtain on the other setup owing to large fluctuations in the NOPA probes around the 800-nm fundamental of the Ti:sapphire laser.

In our TA measurements on the PM6:Y6 blend, the excitation densities created by our 1.8 µJ cm^{-2} pulse at 532 nm are equivalent to 3-Sun operation conditions for PM6:Y6 (about 3×10^{17} cm^{-3})[42]. By contrast, the 9.0 µJ cm^{-2} pulse at 532 nm is equivalent to 15-Sun operation. We intentionally performed our TA measurements at excitation densities in excess of those at 1-Sun, because the increased rate of non-geminate recombination enables us to identify and model the triplet recombination pathways present in the organic solar cell blends studied here. Under 1-Sun conditions, the lower excitation densities increase the time taken to the onset of non-geminate recombination processes that result in T_1 formation, enabling charge carriers to be extracted before substantial recombination losses to T_1 occur. This may explain why the PM6:Y6 devices investigated here (which show particularly efficient charge extraction[42]) demonstrate excellent performance, despite 90% of recombination proceeding via the Y6 T_1 under open-circuit conditions.

trEPR spectroscopy

Triplet states may also be investigated using trEPR measurements, which allow the detection of only spin-polarized triplets, that is, those for which the spin sublevels T_+, T_0 and T_- have non-thermal occupancies[44]. As a result, we observe enhanced absorptive (a) and emissive (e) characters of the EPR transitions, from which the generation mechanism of the triplet may be determined[44]. Triplets produced via non-geminate recombination from free charge have thermal sublevel occupancies and are thus not detectable[20]. Conversely, triplets produced from geminate processes result in sublevel occupancies far from thermal equilibrium and may be readily observed[23,44,45,55–57]. T_1 formation via geminate back charge transfer may be understood in the framework of the spin-correlated radical pair mechanism[58–61], whereby spin mixing first occurs between $^1CTE_0$ and $^3CTE_0$, then by back charge transfer to the molecular triplet sublevels. Depending on the sign of the zero-field splitting D parameter, the overpopulation of either T_0 or T_+/T_- results in an aeeaae or eaaeea spin-polarization pattern of the T_1 trEPR signal, a clear and unique fingerprint of the geminate pathway[23,44,45]. Although performed at 80 K, we expect that these measurements are relevant to the blend behaviour at 293 K. Detailed discussions of the influence of temperature and an in-depth review of EPR theory are provided in Supplementary Information.

EPR samples were fabricated by spin-coating solutions under identical conditions to the optimized devices onto Mylar substrates, which were subsequently cut into strips with a width of 3 mm. To ensure the flexible Mylar substrates did not bend during the spin-coating process, they were mounted onto rigid glass substrates using adhesive tape. The strips were placed in quartz EPR tubes, which were sealed in a nitrogen glovebox with a bicomponent resin (Devcon 5-Minute Epoxy), ensuring that all EPR measurements were performed without oxygen exposure.

All trEPR spectra were recorded on a Bruker Elexsys E580 X-band spectrometer, equipped with a nitrogen-gas-flow cryostat for sample temperature control. The sample temperature was maintained with an Oxford Instruments CF935O cryostat and controlled with an Oxford Instruments ITC503. Laser pulses for trEPR were collimated into the cryostat and resonator windows from a multimode optical fibre, ThorLabs FT600UMT. Sample excitation at 532 nm with an energy of 2 mJ per pulse and a duration of 7 ns was provided by the residual second-harmonic output of a Newport/Spectra Physics Lab 170 Quanta Ray Nd:YAG pulsed laser, operating at 20 Hz. The trEPR signal was recorded through a Bruker SpecJet II transient recorder with timing synchronization by a Stanford Research Systems DG645 delay generator. The instrument response time was about 200 ns. The spectra were acquired with 2-mW microwave power and averaging 400 transient signals at each field position.

The trEPR spectra were recorded by adopting a direct-detection scheme[55]. Specifically, the EPR intensity was recorded as a function of time after laser excitation, with constant applied X-band microwave radiation, for each magnetic field position. We used this configuration because it has a better signal-to-noise ratio than the delay after flash echo-detected experiments at 80 K. Indeed, most triplet states have relaxation times too short to be detectable with the pulsed-detection scheme at 80 K. At lower temperatures (usually 20 K), pulsed detection usually becomes feasible, but the spectra may become complicated owing to several paramagnetic species being present, including thermally populated triplets produced via non-geminate recombination from free-charge carriers and stable states that are not usually observable using direct detection. From the dataset obtained, the trEPR spectrum at different time delays after the laser pulse was extracted. The reported trEPR spectra were averaged over a time window of 1 µs. The acquired trEPR spectra were simulated by using the core functions 'pepper' and 'esfit' of the open-source MATLAB toolbox EasySpin[62]. The parameters included in our best-fit simulations are the ZFS parameters (D and E), the triplet population sublevels (p_1, p_2, p_3) and the line broadening (assumed as only Lorentzian to not over-parameterize the fitting). For the calculation of spin polarization, the populations of the spin-triplet sublevels at zero field were calculated (T_x, T_y, T_z) in the fitting program and used by EasySpin to simulate the trEPR spectrum at resonant fields. For all the simulations, the g tensor was assumed isotropic, with $g_{iso} = 2.002$. To carry out our least-square fittings, a user-defined simulation function was developed, which allowed the fitting of non-spin-system parameters, such as the spin populations of the triplet sublevels. All the fits were carried out using a Nelder/Mead downhill simplex optimization algorithm.

Reporting summary

Further information on research design is available in the Nature Research Reporting Summary linked to this paper.

Data availability

The data that support the plots within this paper and other findings of this study are available at the University of Cambridge Repository (https://doi.org/10.17863/CAM.75316).

51. Rasaiah, J. C., Hubbard, J. B., Rubin, R. J. & Lee, S. H. Kinetics of bimolecular recombination processes with trapping. *J. Phys. Chem.* **94**, 652–662 (1990).
52. Lee, J. et al. Bandgap narrowing in non-fullerene acceptors: single atom substitution leads to high optoelectronic response beyond 1000 nm. *Adv. Energy Mater.* **8**, 1801212 (2018).
53. de Mello, J. C., Wittmann, H. F. & Friend, R. H. An improved experimental determination of external photoluminescence quantum efficiency. *Adv. Mater.* **9**, 230–232 (1997).
54. Lee, C.-L., Yang, X. & Greenham, N. C. Determination of the triplet excited-state absorption cross section in a polyfluorene by energy transfer from a phosphorescent metal complex. *Phys. Rev. B* **76**, 245201 (2007).
55. Biskup, T. Structure-function relationship of organic semiconductors: detailed insights from time-resolved EPR spectroscopy. *Front Chem.* **7**, 10 (2019).
56. Weber, S. Transient EPR. *eMagRes* **6**, 255–270 (2017).
57. Niklas, J. & Poluektov, O. G. Charge transfer processes in OPV materials as revealed by EPR spectroscopy. *Adv. Energy Mater.* **7**, 1602226 (2017).
58. Righetto, M. et al. Engineering interactions in QDs-PCBM blends: a surface chemistry approach. *Nanoscale* **10**, 11913–11922 (2018).
59. Franco, L. et al. Time-resolved EPR of photoinduced excited states in a semiconducting polymer/PCBM blend. *J. Phys. Chem. C* **117**, 1554–1560 (2013).
60. Buckley, C. D., Hunter, D. A., Hore, P. J. & McLauchlan, K. A. Electron spin resonance of spin-correlated radical pairs. *Chem. Phys. Lett.* **135**, 307–312 (1987).
61. Hore, P. J., Hunter, D. A., McKie, C. D. & Hoff, A. J. Electron paramagnetic resonance of spin-correlated radical pairs in photosynthetic reactions. *Chem. Phys. Lett.* **137**, 495–500 (1987).
62. Stoll, S. & Schweiger, A. EasySpin, a comprehensive software package for spectral simulation and analysis in EPR. *J. Magn. Reson.* **178**, 42–55 (2006).

Acknowledgements A.J.G. and R.H.F. acknowledge support from the Simons Foundation (grant number 601946) and the EPSRC (EP/M01083X/1 and EP/M005143/1). This project has received funding from the ERC under the European Union's Horizon 2020 research and innovation programme (grant agreement number 670405). A.K. and T.-Q.N. were supported by the Department of the Navy, Office of Naval Research award number N00014-21-1-2181. A.K. acknowledges funding by the Schlumberger foundation. A.Privitera, R.D., A.Pershin, G.L., M.K.R. and D.B. were supported by the European Union's Horizon 2020 research and innovation programme under Marie Skłodowska Curie grant agreement number 722651 (SEPOMO project). Computational resources in Mons were provided by the Consortium des Équipements de Calcul Intensif (CÉCI), funded by the Fonds de la Recherche Scientifiques de Belgique (FRS-FNRS) under grant number 2.5020.11, as well as the Tier-1 supercomputer of the Fedération Wallonie-Bruxelles, infrastructure funded by the Walloon Region under grant agreement number 1117545. D.B. is a FNRS Research Director. F.G. acknowledges the Stiftelsen för Strategisk Forskning through a Future Research Leader programme (FFL18-0322). Transient electron paramagnetic resonance measurements were performed in the Centre for Advanced ESR (CAESR) in the Department of Chemistry at the University of Oxford, and this work was supported by the EPSRC (EP/L011972/1). We thank T. Biskup and A. Sperlich for their assistance with simulation and interpretation of the transient electron paramagnetic resonance data.

Author contributions A.J.G., T.-Q.N. and R.H.F. conceived the work. A.J.G. performed the transient absorption measurements. A.Privitera and W.K.M. conducted the transient electron paramagnetic resonance measurements. R.D., A.Pershin and G.L. carried out the quantum chemical calculations. A.K., D.Q., J.Y. and S.-J.K. fabricated and tested the organic solar cell devices. A.J.G. and J.Y. performed the photoluminescence quantum efficiency measurements. J.L. synthesized SiOTIC-4F and the IEICO derivatives. M.K.R., F.G., G.C.B., T.-Q.N, D.B. and R.H.F. supervised their group members involved in the project. A.J.G., A.R. and R.H.F. wrote the manuscript, with input from all authors.

Competing interests The authors declare no competing interests.

Additional information

Supplementary information The online version contains supplementary material available at https://doi.org/10.1038/s41586-021-03840-5.

Correspondence and requests for materials should be addressed to Alexander J. Gillett, Thuc-Quyen Nguyen, David Beljonne or Richard H. Friend.

Peer review information *Nature* thanks Till Biskup, Yingping Zou and the other, anonymous, reviewer(s) for their contribution to the peer review of this work.

Reprints and permissions information is available at http://www.nature.com/reprints.

Corresponding author(s): Alexander J. Gillett, Thuc-Quyen Nguyen, David Beljonne and Richard H. Friend

Solar Cells Reporting Summary

Nature Research wishes to improve the reproducibility of the work that we publish. This form is intended for publication with all accepted papers reporting the characterization of photovoltaic devices and provides structure for consistency and transparency in reporting. Some list items might not apply to an individual manuscript, but all fields must be completed for clarity.

For further information on Nature Research policies, including our data availability policy, see Authors & Referees.

Experimental design

Please check: are the following details reported in the manuscript?

1. Dimensions			
Area of the tested solar cells	☒ Yes ☐ No	See Methods; "OSC device fabrication".
Method used to determine the device area	☒ Yes ☐ No	See Methods; "OSC device fabrication".
2. Current-voltage characterization			
Current density-voltage (J-V) plots in both forward and backward direction	☒ Yes ☐ No	See Methods; "OSC device testing".
Voltage scan conditions *For instance: scan direction, speed, dwell times*	☒ Yes ☐ No	See Methods; "OSC device testing".
Test environment *For instance: characterization temperature, in air or in glove box*	☒ Yes ☐ No	See Methods; "OSC device testing".
Protocol for preconditioning of the device before its characterization	☐ Yes ☒ No	The devices were not preconditioned before characterization.
Stability of the J-V characteristic *Verified with time evolution of the maximum power point or with the photocurrent at maximum power point; see ref. 7 for details.*	☐ Yes ☒ No	As the purpose of the study is to investigate voltage losses, no stability measurements were performed.
3. Hysteresis or any other unusual behaviour			
Description of the unusual behaviour observed during the characterization	☐ Yes ☒ No	No unusual behaviour.
Related experimental data	☐ Yes ☒ No	No unusual behaviour.
4. Efficiency			
External quantum efficiency (EQE) or incident photons to current efficiency (IPCE)	☐ Yes ☒ No	As the devices were fabricated primarily to determine the EL efficiency and to demonstrate that the power conversion efficiency is comparable to previous reports of the blends, no EQE measurements were performed.
A comparison between the integrated response under the standard reference spectrum and the response measure under the simulator	☐ Yes ☒ No	As the devices were fabricated primarily to determine the EL efficiency and to demonstrate that the power conversion efficiency is comparable to previous reports of the blends, no comparison was performed.
For tandem solar cells, the bias illumination and bias voltage used for each subcell	☐ Yes ☒ No	No tandem cells reported.
5. Calibration			
Light source and reference cell or sensor used for the characterization	☒ Yes ☐ No	See Methods; "OSC device testing".
Confirmation that the reference cell was calibrated and certified	☒ Yes ☐ No	See Methods; "OSC device testing".

Calculation of spectral mismatch between the reference cell and the devices under test	☐ Yes ☒ No	As the devices were fabricated primarily to determine the EL efficiency and to demonstrate that the power conversion efficiency is comparable to previous reports of the blends, we did not calculate the spectral mismatch.

6. Mask/aperture

Size of the mask/aperture used during testing	☐ Yes ☒ No	As the devices were fabricated primarily to determine the EL efficiency and to demonstrate that the power conversion efficiency is comparable to previous reports of the blends, we did not measure the devices with a mask.
Variation of the measured short-circuit current density with the mask/aperture area	☐ Yes ☒ No	As the devices were fabricated primarily to determine the EL efficiency and to demonstrate that the power conversion efficiency is comparable to previous reports of the blends, we did not measure the devices with a mask.

7. Performance certification

Identity of the independent certification laboratory that confirmed the photovoltaic performance	☐ Yes ☒ No	As the purpose of the study is to investigate voltage losses in previously-reported blends, the efficiency values were not certified.
A copy of any certificate(s) *Provide in Supplementary Information*	☐ Yes ☒ No	No certification performed.

8. Statistics

Number of solar cells tested	☒ Yes ☐ No	See Methods; "OSC device testing".
Statistical analysis of the device performance	☒ Yes ☐ No	See Methods; "OSC device testing".

9. Long-term stability analysis

Type of analysis, bias conditions and environmental conditions *For instance: illumination type, temperature, atmosphere humidity, encapsulation method, preconditioning temperature*	☐ Yes ☒ No	As the purpose of the study is to investigate voltage losses, no stability measurements were performed.